

Metal-to-metal communication during the spin state transition of a [2x2] Fe(II) metallogrid at equilibrium and out-of-equilibrium conditions

Jose de Jesus Velazquez-Garcia^{a*}, Krishnayan Basuroy^a, Darina Storozhuk^a, Joanne Wong^b, Serhiy Demeshko^b, Franc Meyer^b, Robert Henning^c and Simone Techert^{ad}

^aPhoton Science - Structural Dynamics in Chemical Systems, Deutsches Elektronen-Synchrotron DESY, Notkestraße 85, Hamburg, 22607, Germany

^bInstitut für Anorganische Chemie, Georg-August-Universität Göttingen, Tammannstraße 4, Göttingen, 37077, Germany

^cCenter for Advanced Radiation Sources, The University of Chicago, Argonne National Laboratory, 9700 South Cass Ave, Lemont, Illinois, 90439, USA

^dInstitut für Röntgenphysik, Georg-August-Universität Göttingen, Friedrich-Hund-Platz 1, Göttingen, 37077, Germany

Synthesis

The complex grid **FE4** and its ligand were synthesized following the procedure reported in literature¹. The crystallographic data for this paper can be obtained free of charge from The Cambridge Crystallographic Data Centre via www.ccdc.cam.ac.uk/data_request/cif. Deposition numbers:

FE4 from 100 K to 390 K: 2126240, 2127042-2127051, 2127052-2127057 and 2127059-2127064.

Time resolved: 2127311-2127319.

Vibrational spectroscopy

The infrared spectra in the 2000-2500 cm⁻¹ range of the original and desolvated **FE4** grid are shown in Figure S6. The presence of acetonitrile in the original **FE4** sample is confirmed by the appearance of two distinctive signals: $\nu(\text{C}\equiv\text{N})$ at 2249 cm⁻¹ and a combined band of $\nu(\text{C}-\text{C})+\delta(\text{CH}_3)$ at 2293 cm⁻¹²⁻⁵. In contrast, the desolvated **FE4** grid did not display the aforementioned bands, which indicate a complete desolvation.

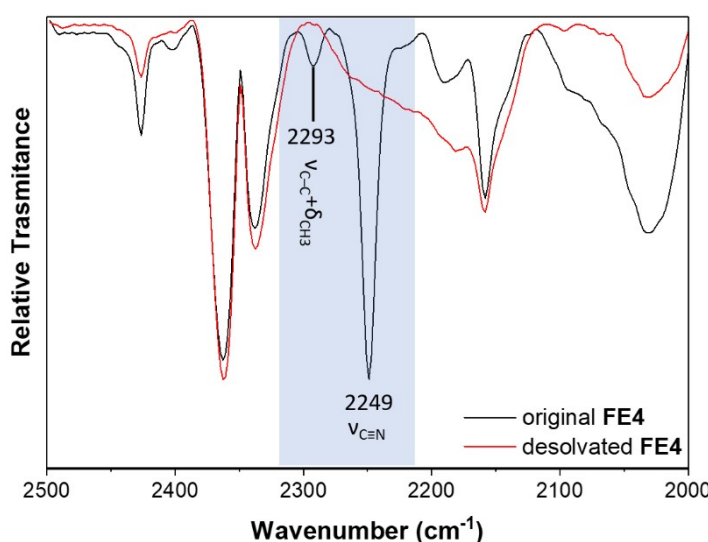


Figure S1. FTIR spectra for original and desolvated **FE4** grid.

Characterization

Table S1. Crystal data and structure refinement parameters of **FE4** at 100 K.

Temperature	100 K
Empirical Formula	C100 H74 B4 F16 Fe4 N26
Crystal color/habit	Black/block
Crystal size (mm)	(0.090x0.120x0.050)
Crystallizing solvent	Acetonitrile
Crystal system/ Space group	Monoclinic/ C2/c
<i>a</i> (Å)	30.680 (6)
<i>b</i> (Å)	12.780 (3)
<i>c</i> (Å)	26.810 (5)
α (°)	90
β (°)	120.76 (3)
γ (°)	90
Volume (Å ³)	9107.0 (4)
<i>Z/Z'</i>	4/0.5
Molecular Weight	2210.49
Calculated density (g/cm ³)	
F(000)	1.625
Radiation	Synchrotron ($\lambda=0.61990 \text{ \AA}$)
θ range (°)	1.902/31.355
Scan type	φ
Measured reflections	48052
Unique reflections	14709
Observed reflections	13786
[F > 4σ(F)]	
Final R (%)	5.03
wR2 (%)	14.88
Good-of-fit on F ² (S)	1.086
Δρ max (e. Å ⁻³)	0.794
Δρ min (e. Å ⁻³)	-0.696
No of restraints/parameters	90/751
Data [F > 4σ(F)]-to-parameter ratio	18.35:1

Table S2. Selected bond lengths and bond angles for compound **FE4** at 100K.

Bond lengths (Å)		Bond angles (°)			
Fe(A)-N2	1.9030(12)	N2-Fe(A)-N5	172.81(5)	N7-Fe(B)-N10	100.60(5)
Fe(A)-N5	1.9036(12)	N2-Fe(A)-N00	80.53(6)	N7-Fe(B)-N11	129.94(5)
Fe(A)-N00	1.9893(14)	N5-Fe(A)-N00	95.49(6)	N10-Fe(B)-N11	76.23(5)
Fe(A)-N3	1.9898(13)	N2-Fe(A)-N3	80.08(6)	N7-Fe(B)-N8	76.59(6)
Fe(A)-N4	1.9949(12)	N5-Fe(A)-N3	103.96(6)	N10-Fe(B)-N8	128.36(5)
Fe(A)-N6	1.9953(11)	N00-Fe(A)-N3	160.55(5)	N11-Fe(B)-N8	143.82(6)
Fe(B)-N7	2.1203(14)	N2-Fe(A)-N4	94.07(5)	N7-Fe(B)-N12	90.50(5)
Fe(B)-N10	2.1327(13)	N5-Fe(A)-N4	80.37(5)	N10-Fe(B)-N12	146.11(5)
Fe(B)-N11	2.1331(13)	N00-Fe(A)-N4	96.60(5)	N11-Fe(B)-N12	72.20(5)
Fe(B)-N8	2.1413(13)	N3-Fe(A)-N4	86.31(5)	N8-Fe(B)-N12	85.27(5)
Fe(B)-N12	2.2799(14)	N2-Fe(A)-N6	105.09(5)	N7-Fe(B)-N9	147.01(5)
Fe(B)-N9	2.3278(17)	N5-Fe(A)-N6	80.30(5)	N10-Fe(B)-N9	92.69(6)
		N00-Fe(A)-N6	84.10(5)	N11-Fe(B)-N9	82.44(5)
		N3-Fe(A)-N6	99.48(5)	N8-Fe(B)-N9	71.53(6)
		N4-Fe(A)-N6	160.64(5)	N12-Fe(B)-N9	95.07(6)

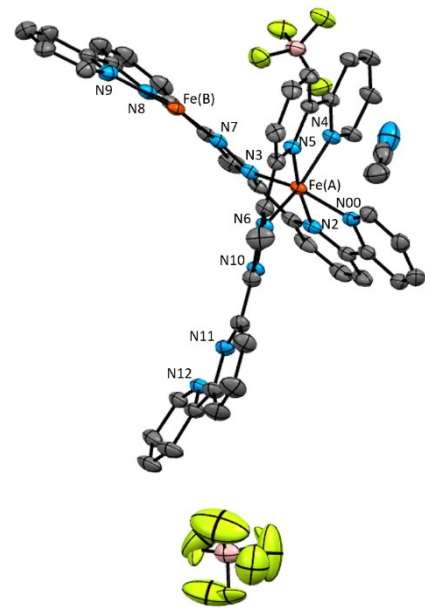


Figure S2. Asymmetric unit of the **FE4** grid at 100K. Hydrogen were omitted for clarity.

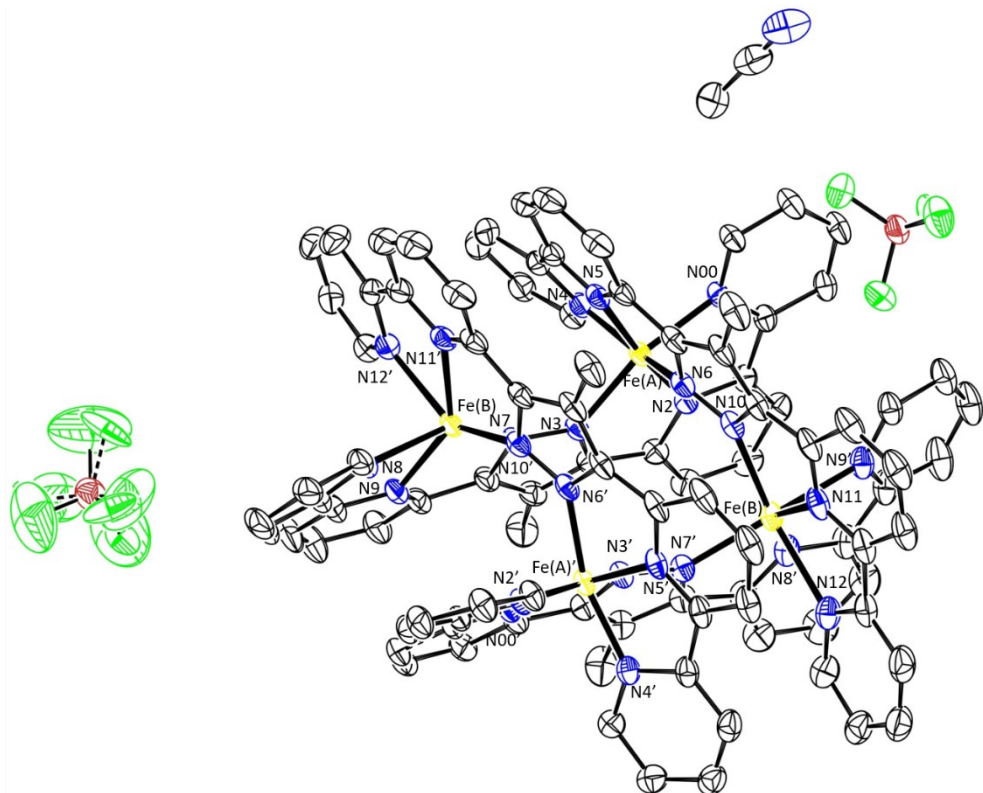


Figure S3. Thermal ellipsoid plot (50% of probability) for **FE4** at 100K.

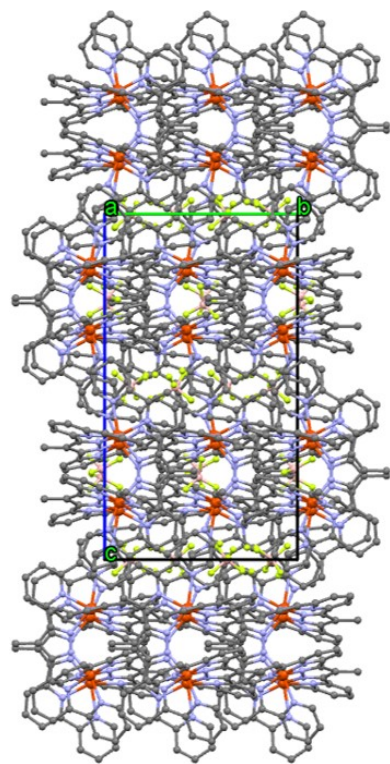


Figure S4. Packing of molecules down crystallographic ‘*a*’ axis. Hydrogen atoms are omitted for clarity.

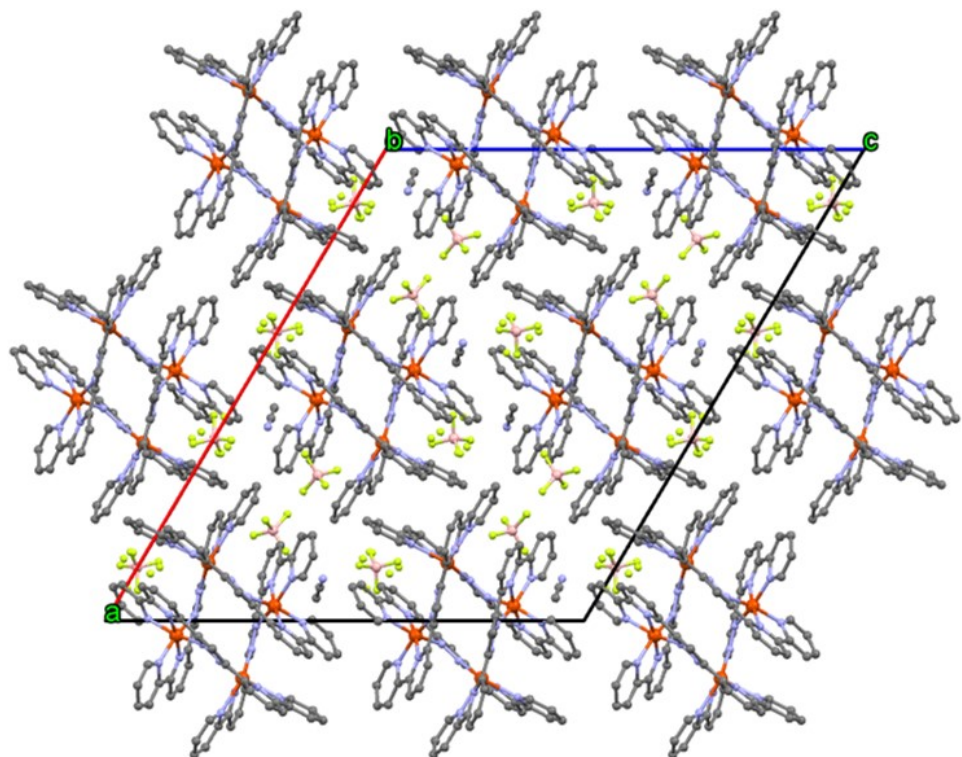


Figure S5. Packing of molecules down crystallographic ‘*b*’ axis. Hydrogen atoms are omitted for clarity.

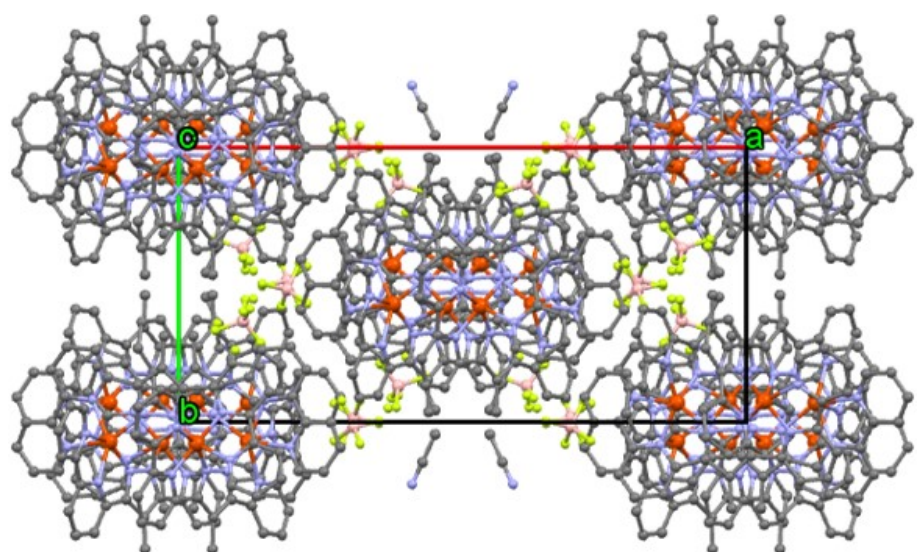


Figure S6. Packing of molecules down crystallographic 'c' axis. Hydrogen atoms are omitted for clarity.

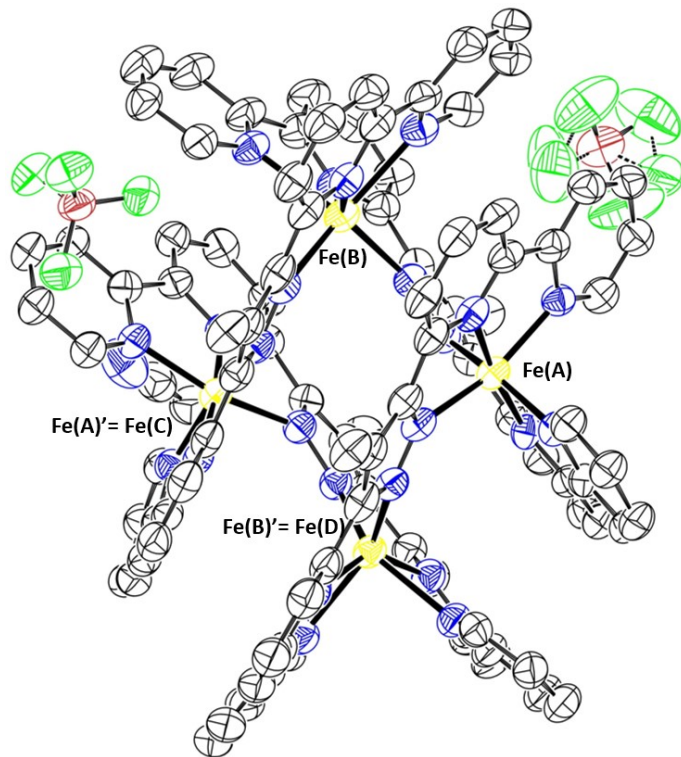


Figure S7. Thermal ellipsoid plot (50% of probability) for **FE4** for the -5ns data.

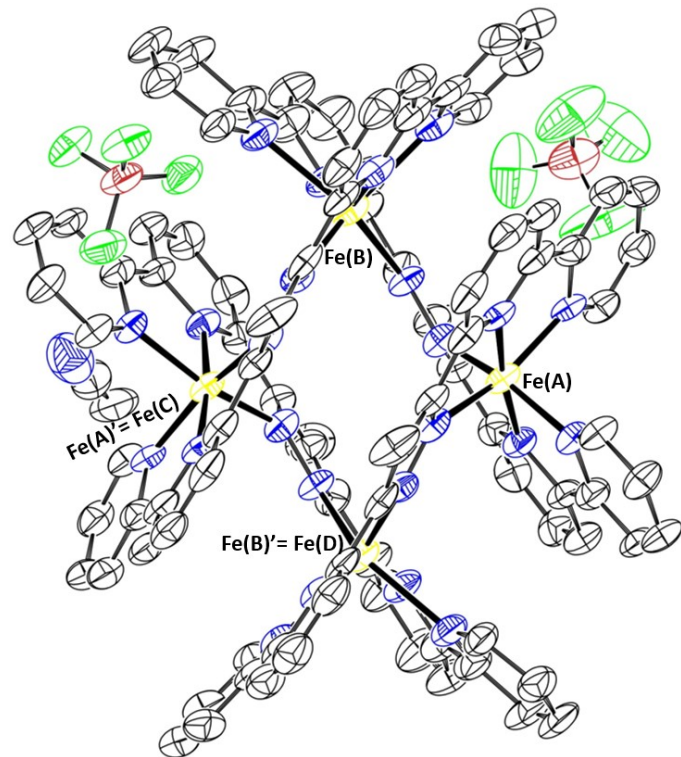


Figure S8. Thermal ellipsoid plot (50% of probability) for **FE4** for the -2ns data.

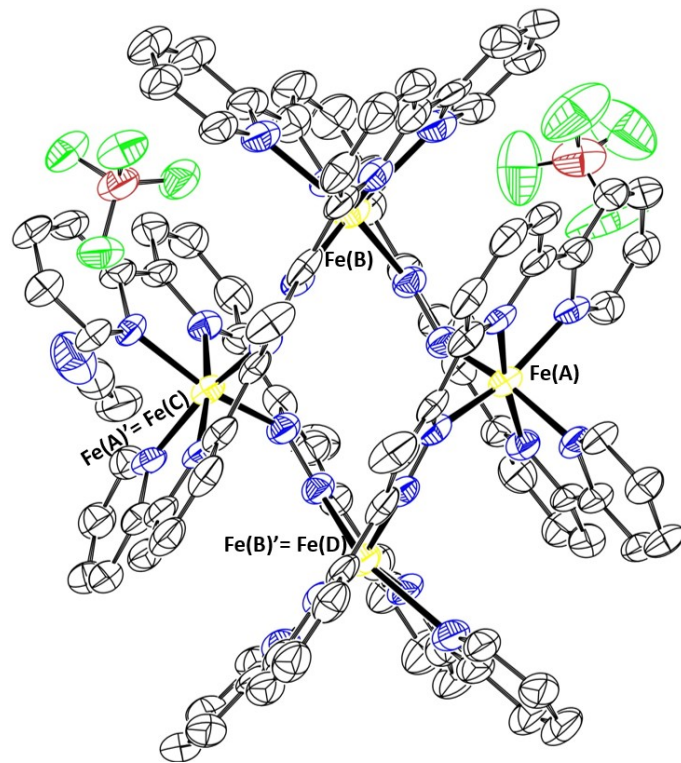


Figure S9. Thermal ellipsoid plot (50% of probability) for **FE4** for the -200ps data.

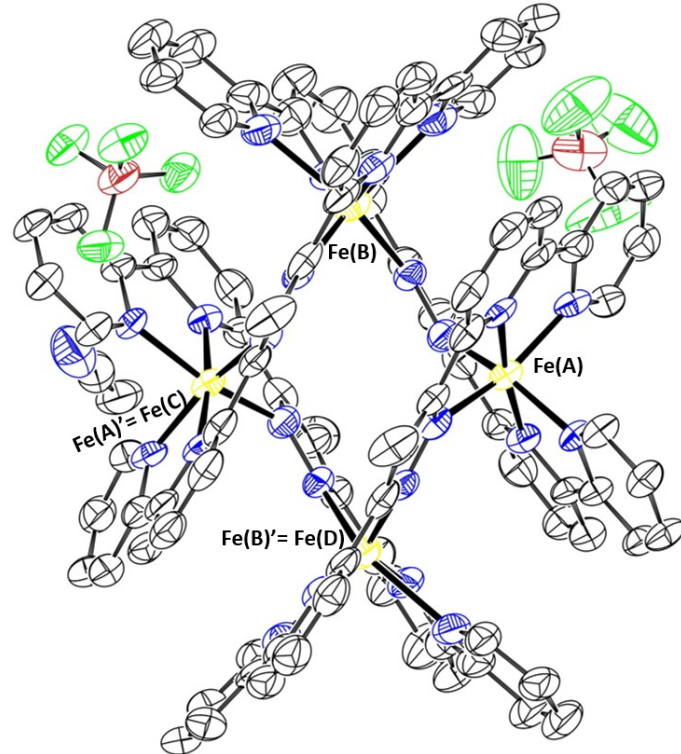


Figure S10. Thermal ellipsoid plot (50% of probability) for **FE4** for the 100ps data.

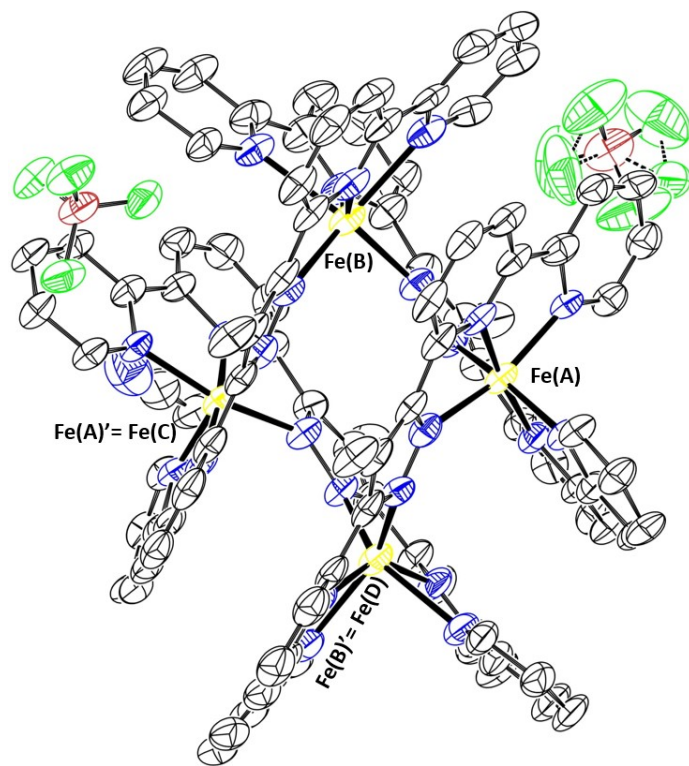


Figure S11. Thermal ellipsoid plot (50% of probability) for **FE4** for the 200ps data.

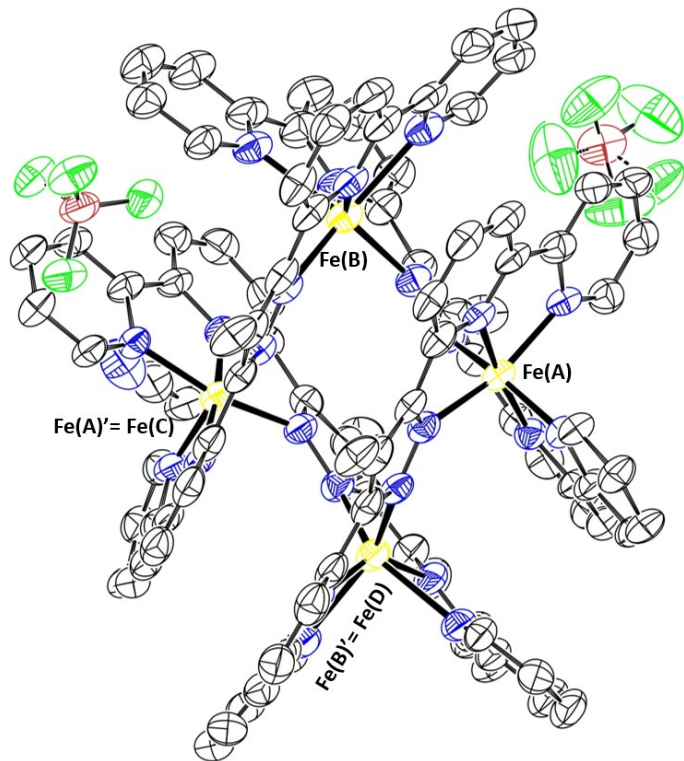


Figure S12. Thermal ellipsoid plot (50% of probability) for **FE4** for the 500ps data.

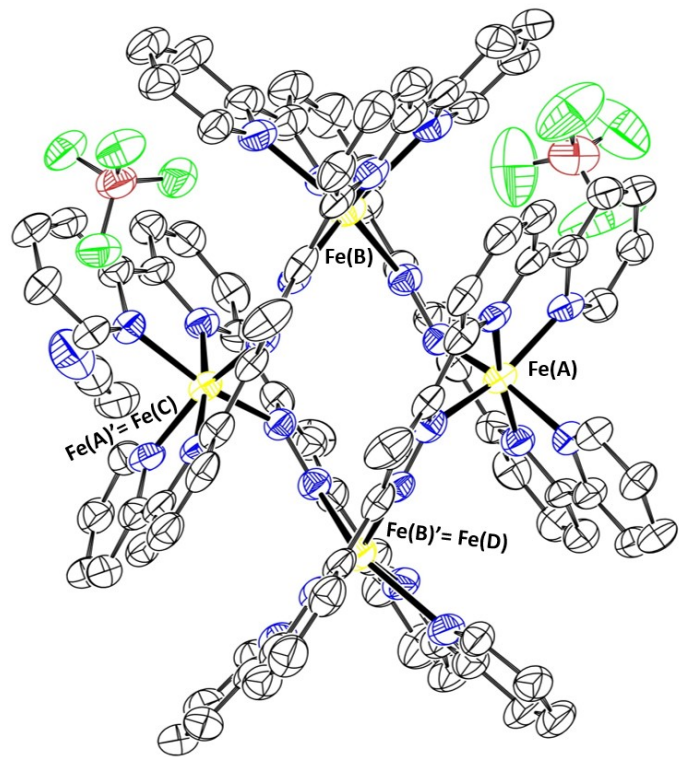


Figure S13. Thermal ellipsoid plot (50% of probability) for **FE4** for the 1ns data.

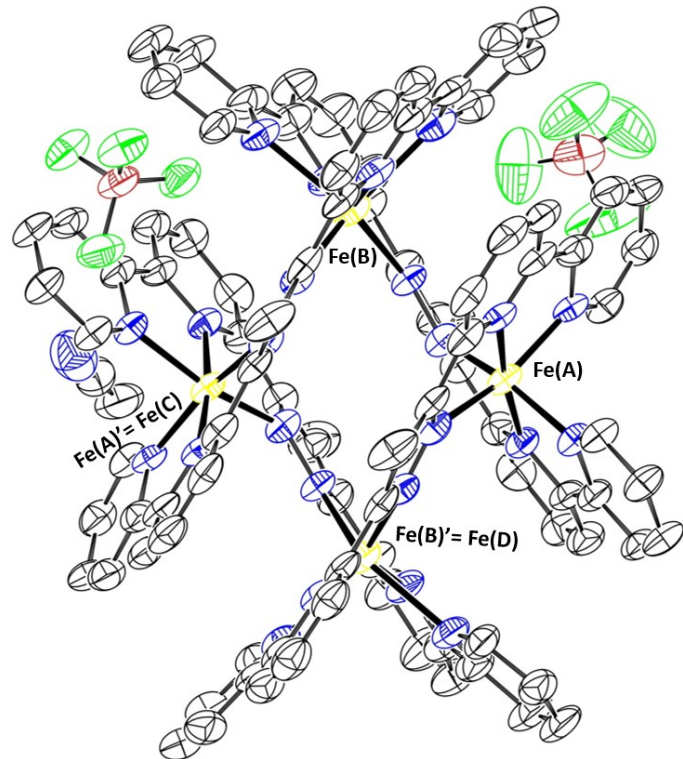


Figure S14. Thermal ellipsoid plot (50% of probability) for **FE4** for the 2ns data.

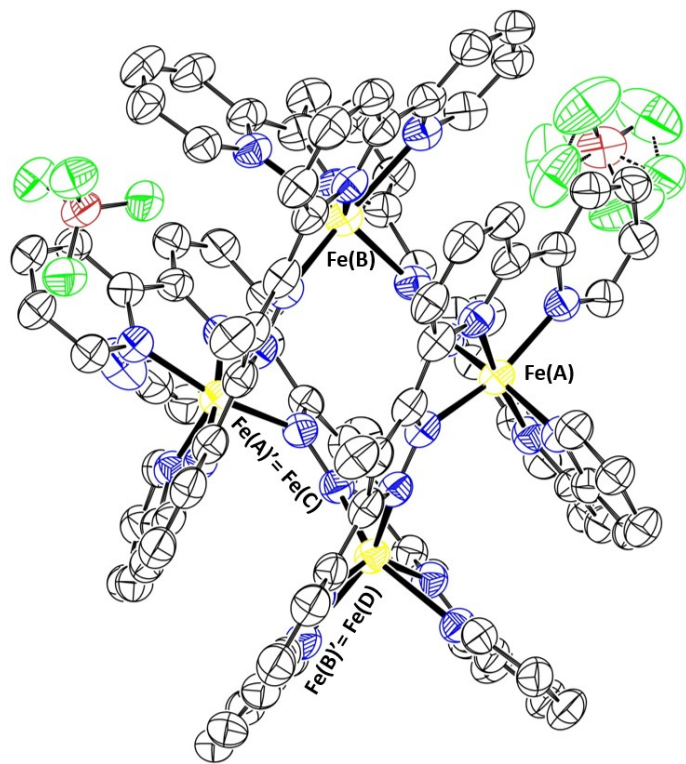
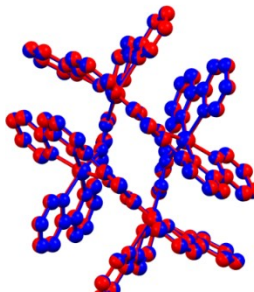
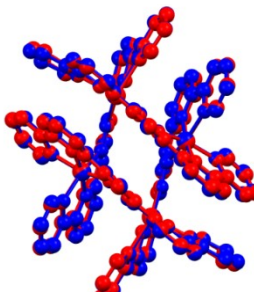
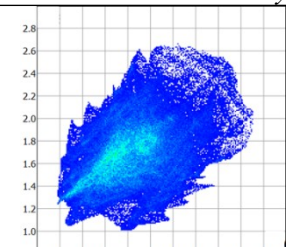
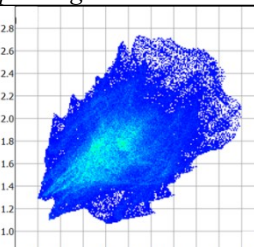
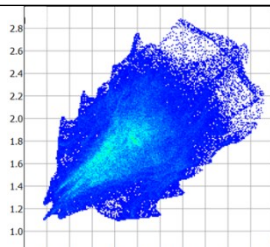


Figure S15. Thermal ellipsoid plot (50% of probability) for **FE4** for the 5ns data.

Structural details

Table S3. Structural data that provides a basic description of the SCO in **FE4**

Structural parameter	100 K	290 K	390 K
<i>Fe(A)-N6 polyhedron</i>			
<Fe1-N> (Å)	1.96 (2)	1.97 (2)	2.02 (2)
S(Oh)	2.315	2.390	3.098
S(itp)	10.529	10.386	9.421
Σ (°)	103.01 (8)	102.66 (13)	113.40 (13)
Θ (°)	306.7425	311.7653	368.8379
ζ (Å)	0.24 (5)	0.25 (5)	0.25 (6)
Vp (Å³)	9.68	9.834	10.426
<i>Fe(B)-N6 polyhedron</i>			
<Fe2-N> (Å)	2.19 (4)	2.20 (4)	2.20 (4)
S(Oh)	8.401	8.444	8.902
S(itp)	4.417	4.408	4.290
Σ (°)	172.95 (8)	172.88	177.64 (12)
Θ (°)	708.9869	709.6041	734.0074
ζ (Å)	0.46 (9)	0.48 (9)	0.47 (9)
Vp (Å³)	11.835	11.931	11.919
<i>Molecular Scale</i>			
Superposition of structures	100K (blue) & 290 K (red)	100K (blue) & 390 K (red)	
			
Maximum RMSD	0.1124	0.2356	
Average RMSD	0.0465	0.1206	
<i>Unit cell Changes</i>			
a (Å)	31.330 (6)	31.100 (6)	31.330 (6)
b (Å)	12.780 (3)	12.870 (3)	12.960 (3)
c (Å)	26.810 (6)	27.360 (6)	27.500 (6)
V (Å³)	9033 (4)	9377 (4)	9551 (4)
<i>Crystal packing</i>			
Intermolecular interactions			
Separation between π - π planes (Å)	3.444, 4.503	3.509, 4.665	3.565, 4.769
Crystal density	1.571	1.513	1.486

$\Sigma = \sum_{i=1}^{12} |90 - \phi_i|$, the sum of the angular deviations from 90° for the 12 cis angles (ϕ_i)^{6,7}, $\Theta = \sum_{i=1}^{24} |60 - \theta_i|^8$, $\zeta = (\text{Fe}-\text{N}_i) - \langle \text{Fe}-\text{N} \rangle^9$. Information about S(Oh) and S(itp) is provided in the structural analysis section.

Structural Analysis

The Octadist program¹⁰ was used to determine the $\langle \text{Fe-N} \rangle$ bond length and the angular distortion parameter that describe the octahedral coordination environment of the metal centres in the **FE4** grid. The angular distortion parameter, Θ , is the sum of the deviations from 60° of the twenty-four N-Fe-N angles, six per pseudo three-fold axis, measured on a projection of opposite triangular faces of the $\{\text{FeN}_6\}$ octahedron, orientated by superimposing the face centroids (Figure S16).^{8,11}

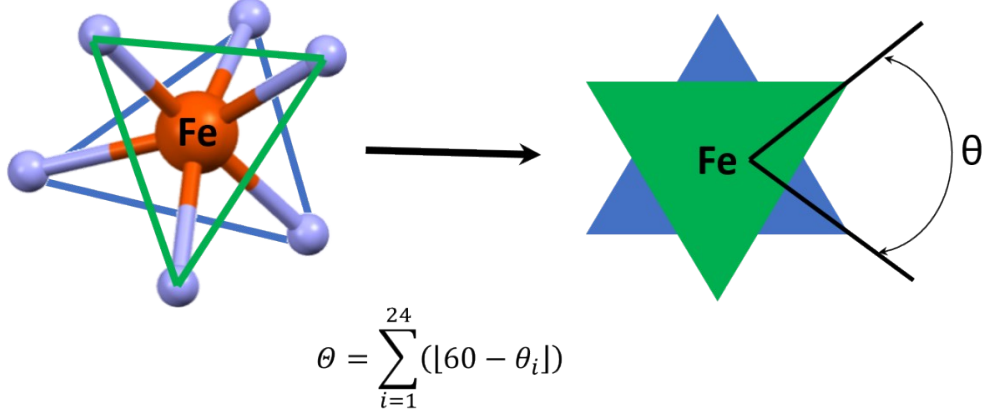


Figure S16. Environment of Fe^{II} ions and definition of the θ angle and the angular distortion parameter (Θ).^{8,11}

For comparison, continuous shape measurements (CShM) were also used to characterise the relative deviation of the metal coordination spheres in **FE4** from ideal polyhedra described by a particular point symmetry group (Table S2).¹² Mathematically, CShM of the coordination polyhedron Q with the geometric centre \vec{q}_0 relative to an ideal polyhedron P is expressed as:

$$S_Q = \min \left[\frac{\sum_{i=1}^N |\vec{q}_i - \vec{p}_i|^2}{\sum_{i=1}^N |\vec{q}_i - \vec{q}_0|^2} \right] \times 100 \quad (\text{S1})$$

where \vec{q}_i and \vec{p}_i are the position vectors for atoms of two polyhedral. CShM relative to an ideal octahedron (S(Oh)) and an ideal trigonal prism (S(itp)) were calculated using the SHAPE program¹³. The calculation of S(Oh) and S(itp) were performed for all crystallographic-symmetry independent metal atoms.

It is well-known that the $\{\text{FeN}_6\}$ coordination sphere of LS Fe^{II} ions is more regular, i.e., closer to an ideal octahedron. Therefore, the S(Oh) parameter is small and closer to 0, while the parameter S(itp) $\gg 0$. Contrary, Fe^{II} ions in the HS state are characterised by a more irregular structure with structural parameters S(Oh) $\gg 0$ and S(itp) closer to zero.

Temperature difference

The well-known Wilson plot¹⁴ is frequently used to estimate the scale factor, k_s , and the overall isotropic temperature factor (B) of a data set. This plot can be obtained by statistical comparison of the observed

intensities (I_{obs}) with the average squared structure factor equals $\sum_{i=1}^M f_i^2$ for each $\sin \theta/\lambda$ range according to:

$$\ln \left(\frac{I_{obs}}{\sum_{i=1}^M f_i^2} \right) = \ln (k_s) - 2B(\sin \theta/\lambda)^2 \quad (S2)$$

Where M is the number of atoms and f_i is the scattering factor of the ith atom.

The change in the overall isotropic temperature factor (ΔB) between two data sets at different temperature can be estimated from modified Wilson plots. The plots are obtained by a scale-factor refinement of the low temperature data (e.g. 100K) with the high-temperature data (e.g. 290K) structural model and plotting the $\ln(I^{100K}/I^{290K})$. The slope of the dependence of $\ln(I^{100K}/I^{290K})$ with $(\sin \theta/\lambda)^2$ gives the overall increase of isotropic atomic motion, ΔB (equation S3), which is associated with temperature difference between the data sets.¹⁵

$$\ln \left(\frac{I^{100K}}{I^{290K}} \right) = -2\Delta B^{100K - 290K} (\sin \theta/\lambda)^2 \quad (S3)$$

The greater the temperature difference between data sets the greater the value of ΔB , that means a more negative slope of the plot. This feature is used to analyse the temperature increase during the photo-crystallographic experiments as explain below.

During the photo-crystallographic experiments, the energy deposited by the laser pulse largely exceed the energy necessary for the LS to HS transition, which results in some heat diffusion and global warming. A modified Wilson plot, known as photo-Wilson plot (Fig. S17), is then used to estimate the lase-induced temperature increase due to heat dissipation, in a similar way as described above for the temperature-Wilson plots. From the photo-Wilson plot is possible to calculate the variation of the isotropic temperature factor between the data sets at time “t” and the reference data at time $t < 0$ ($\Delta B^{t-t < 0}$):¹⁵

$$\ln \left(\frac{I^{dt}}{I^{dt < 0}} \right) = -2\Delta B^{dt - dt < 0} (\sin \theta/\lambda)^2 \quad (S4)$$

where, I^{dt} and $I^{dt < 0}$ are the observed intensities of data sets at delay time “dt” and the reference data at delay time $dt < 0$. Note that both the thermal-Wilson plot and the photo-Wilson plot were brought to the same scale before calculating the value of ΔB . For more information about this topic, the reader is referred to the literature¹⁵.

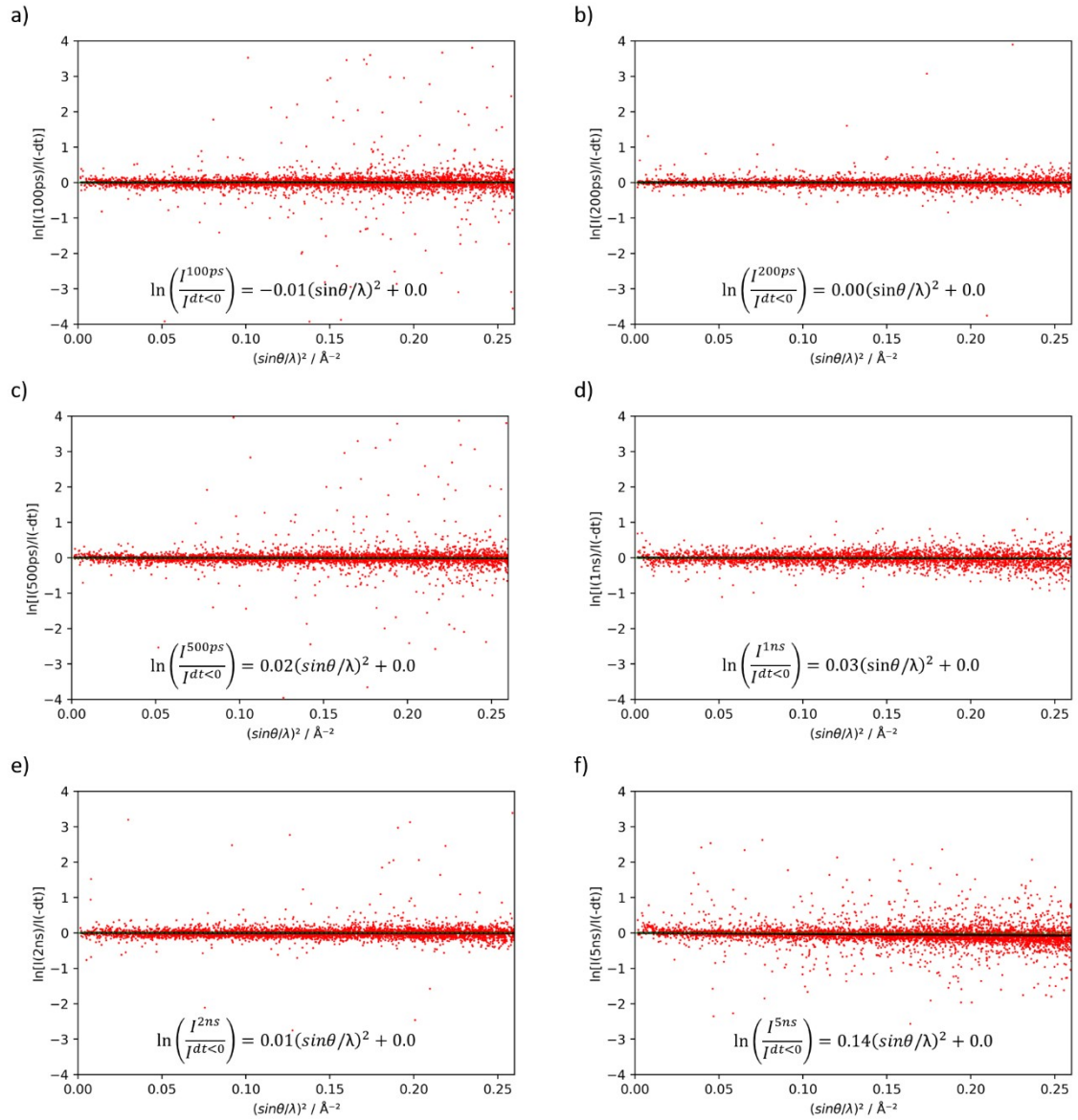


Figure S17. PhotoWilson plots of **FE4**

References

- 1 B. Schneider, S. Demeshko, S. Neudeck, S. Dechert and F. Meyer, *Inorg. Chem.*, 2013, **52**, 13230–13237.
- 2 G. Busca, T. Montanari, M. Bevilacqua and E. Finocchio, *Colloids Surf. Physicochem. Eng. Asp.*, 2008, **320**, 205–212.
- 3 M. P. Marzocchi and S. Dobos, *Spectrochim. Acta Part Mol. Spectrosc.*, 1974, **30**, 1437–1444.
- 4 N. S. Marinković, M. Hecht, J. S. Loring and W. R. Fawcett, *Electrochimica Acta*, 1996, **41**, 641–651.
- 5 P. Schärringer, T. E. Müller, A. Jentys and J. A. Lercher, *J. Catal.*, 2009, **263**, 34–41.
- 6 P. Guionneau, M. Marchivie, G. Bravic, J.-F. Létard and D. Chasseau, in *Spin Crossover in Transition Metal Compounds II*, eds. P. Gütlich and H. A. Goodwin, Springer Berlin Heidelberg, Berlin, Heidelberg, 2004, pp. 97–128.
- 7 M. A. Halcrow, *Chem. Soc. Rev.*, 2011, **40**, 4119.
- 8 M. Marchivie, P. Guionneau, J.-F. Létard and D. Chasseau, *Acta Crystallogr. B*, 2005, **61**, 25–28.
- 9 M. Buron-Le Cointe, J. Hébert, C. Baldé, N. Moisan, L. Toupet, P. Guionneau, J. F. Létard, E. Freysz, H. Cailleau and E. Collet, *Phys. Rev. B*, DOI:10.1103/PhysRevB.85.064114.
- 10 R. Ketkaew, Y. Tantirungrotechai, P. Harding, G. Chastanet, P. Guionneau, M. Marchivie and D. J. Harding, *Dalton Trans.*, 2021, **50**, 1086–1096.
- 11 M. Marchivie, P. Guionneau, J.-F. Létard and D. Chasseau, *Acta Crystallogr. B*, 2003, **59**, 479–486.
- 12 H. Zabrodsky, S. Peleg and D. Avnir, *J. Am. Chem. Soc.*, 1992, **114**, 7843–7851.
- 13 M. Llunell, D. Casanova, J. Cirera, P. Alemany and S. Alvarez, *SHAPE program, version 2.1*, Barcelona, 2003.
- 14 A. J. C. WILSON, *Nature*, 1942, **150**, 152–152.
- 15 M. S. Schmøkel, R. Kamiński, J. B. Benedict and P. Coppens, *Acta Crystallogr. A*, 2010, **66**, 632–636.